THE NEW GLOBAL ICOSAHEDRAL-HEXAGONAL GRIDPOINT MODEL GME OF THE DEUTSCHER WETTERDIENST

D. Majewski
Deutscher Wetterdienst, Offenbach, Germany

1. INTRODUCTION

The current operational global model GM of the Deutscher Wetterdienst (DWD) has been derived from the spectral model of the European Centre for Medium-Range Weather Forecasts (ECMWF) in 1989. Because this model, called cycle 34 at ECMWF, has been coded for shared memory parallel vector processors (PVP) and was not ported to other computer architectures, DWD decided in 1995 to design a new global model for future high-performance computing platforms. This new model will replace GM and the current operational regional model for central Europe EM, therefore, it has been named GME.

Although the spectral method of GM is highly accurate for planetary scale modelling, it suffers from some intrinsic disadvantages which become more apparent as the horizontal resolution increases and the physical parameterization packages gain in complexity.

- Due to the Gibbs phenomenon "spectral ringing" may occur which makes the method unsuitable for positive-definite quantities like cloud liquid water or turbulent kinetic energy which are characterised by steep local gradients. The same is true even for topography which shows unphysical hills and valleys over the oceans after spectral transformation.
- The cost of the Legendre transform increases drastically at higher spectral resolutions, e.g. from about 7% at T_L319 to 20% of the total CP-requirement at T_L639 for the IFS/ARPEGE system jointly developed by ECMWF and Météo France.
- The spectral transforms between Gaussian grid, Fourier space and spectral space require the global communication of large data quantities at each model time step. On modern distributed memory massively parallel computers (MPP systems) this huge global communication requirement is a potential drawback and may inhibit efficient use of the resources available.
- More philosophically, weather prediction can be viewed as the simulation of the local response to local forcing. Thus global basis functions may not provide the best answer in the end.

Therefore, it was decided to base the design of GME on a gridpoint method. But on the other hand, the use of regular latitude-longitude grids on the sphere is restricted with respect to accuracy and efficiency because of the *pole problem*. The convergence of the meridians near the poles results in a clustering of gridpoints which limits the stable time step for explicit or semi-implicit methods severely unless strong artificial damping (Fourier filtering) of short waves is introduced. The use of semi-Lagrangian advection schemes

(e.g. *Staniforth and Côté*, 1991) can overcome this limit as this method is stable even for large Courant numbers. But still the convergence of the meridians in uniform latitude-longitude grids may create a number of problems; for a global model with a mesh size of about 60 km at the equator the mesh size is less than 1 km close to the poles. This small grid distance may result in difficulties for hydrostatic models due to the neglect of nonhydrostatic effects which should be included at this horizontal resolution. Moreover, physical parameterization schemes may be unable to handle the strong inhomogenity of the resolution in physical space. Therefore, an alternative grid which has a more uniform resolution over the globe is being used in GME.

The outline of the paper is as follows: Section 2 describes the grid generation in some detail. The finite-difference operators needed to discretize the atmospheric equations are defined in section 3. The accuracy of the gradient and Laplace operators is evaluated in section 4 by use of a test function proposed by *Heikes and Randall* (1995 b). The two-dimensional version of GME is described and some results for test cases 5 and 6 of the classical shallow water test suite (*Williamson et al.*, 1992) are presented in section 5. The three-dimensional version of GME including dynamics, physical parameterizations, initialization as well as some computational aspects is described in section 6. Results of a detailed evaluation based on the Held-Suarez-Forcing (*Held and Suarez*, 1994) of the dynamical core of the three-dimensional code are given in section 7. Finally, first results of the full model including all physical parameterizations are presented in section 8.

2. GENERATION OF THE MODEL GRID

The icosahedral-hexagonal grid first introduced in meteorological modelling by *Sadourny et al.* (1968) and *Williamson* (1968) gained in popularity in recent years, e.g. *Masuda and Ohnishi* (1987), *Heikes and Randall* (1995 a, b), *Giraldo* (1997) and *Thuburn* (1997). The approach described here closely follows the work of *Baumgardner* (1983) who is using this grid for a three-dimensional finite element model for mantle convection.

To generate the grid mesh, a regular icosahedron (Fig. 1) is placed into the sphere. It touches the sphere at the north and south poles as well as at ten additional points. Five of these points are situated at a longitudinal distance of 72° (= 360°/5) at latitude circle 26.565°N, the other five at 26.565°S. These twelve *special* points are connected by great circle arcs resulting in 20 major spherical triangles (Fig. 2, top left). Given a grid of spherical triangles, a new finer grid of triangles is generated by connecting the midpoints of the existing spherical triangle edges by great circle arcs (Fig. 2, top right and bottom).

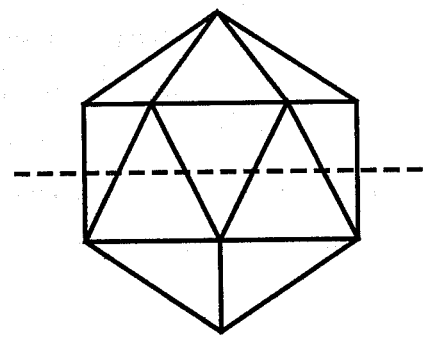

Figure 1 Regular icosahedron which consists of 20 equilateral triangles.

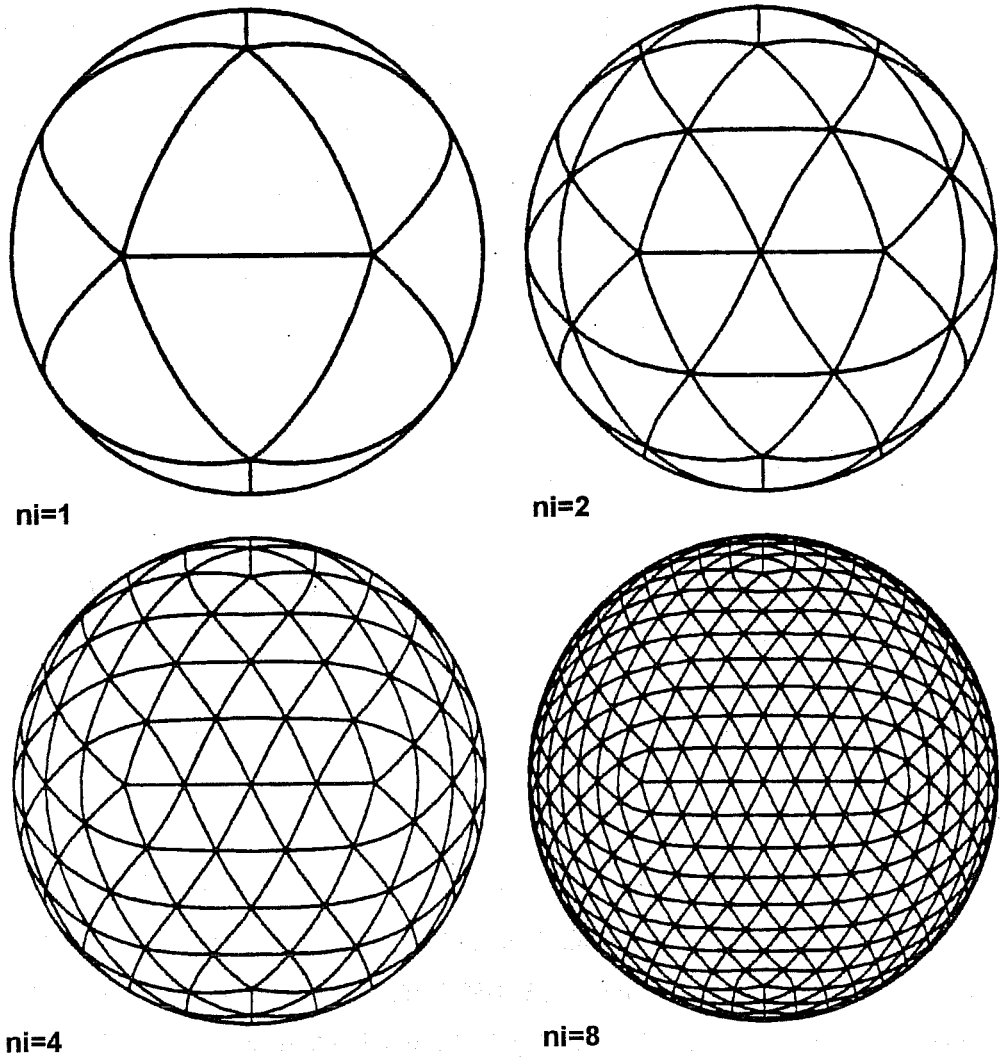

Figure 2 Grid generation by successively halving the triangle edges to form new triangles. Parameter *ni* is the number of intervals on a major triangle edge (length ~ 7054 km).

The new vertices form the additional gridpoints at this refinement step. This process may be repeated until the desired resolution has been reached. The parameter *ni*, i.e. the number of intervals on a major triangle edge (of a length of about 7054 km), is a rough measure of the resolution of the grid. Placing the model variables at the triangle vertices the global grid consists of $2 + 10\ ni^2$ gridpoints (nodes) and $20\ ni^2$ elementary spherical triangles. Each gridpoint corresponds to a hexagon (Fig. 3) or pentagon at the twelve special points.

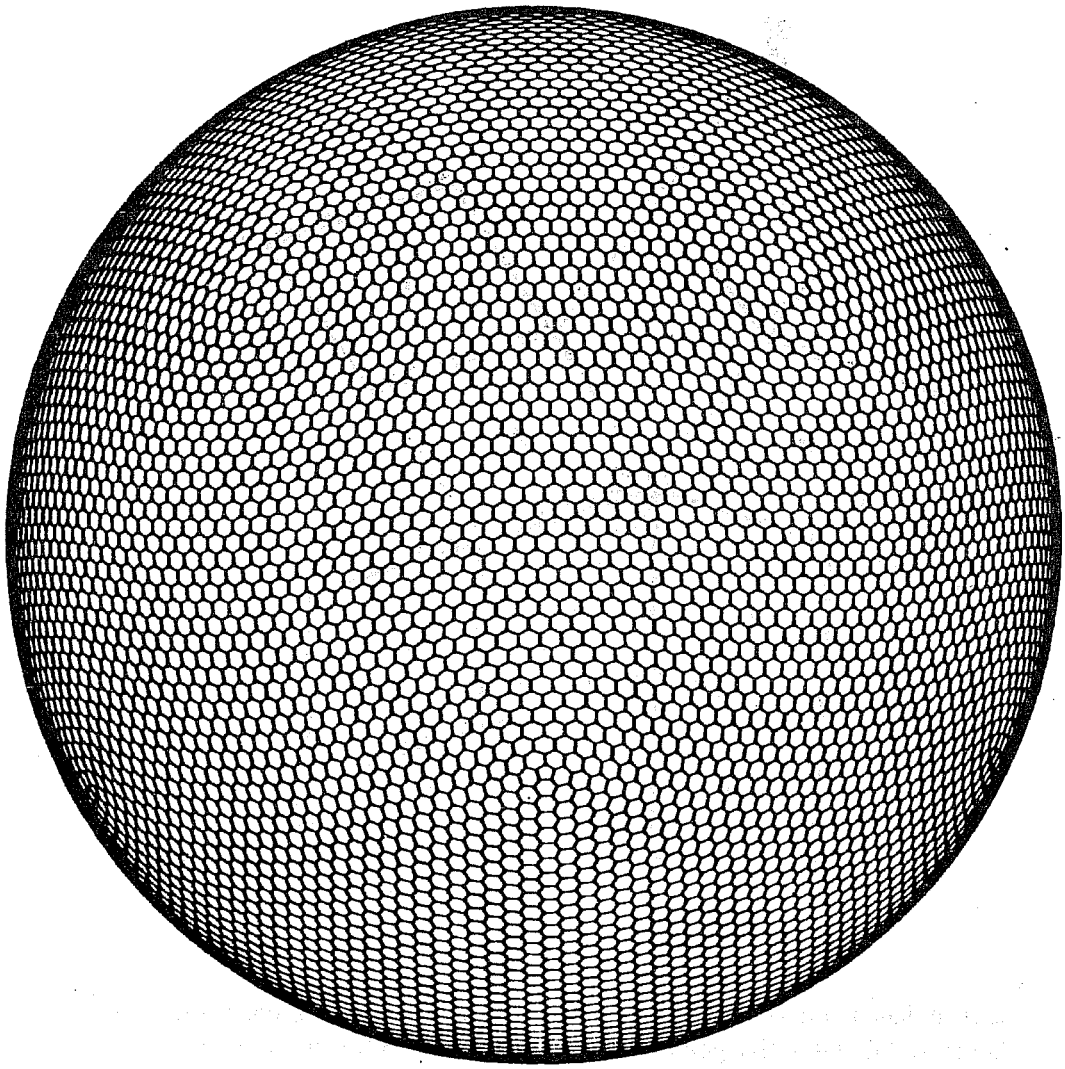

Figure 3 The gridpoints of GME represent nearly uniform hexagons (pentagons at the twelve special points); in this figure, there are three pentagons visible.

The icosahedral-hexagonal grid allows a nearly uniform coverage of the sphere even though the hexagonal grid boxes vary somewhat in their exact shape and size (Tab. 1a), especially those close to the pentagons. The pentagons, however, are perfectly regular, and there is a fivefold symmetry to any one of the 12 pentagons. The mesh size is defined as the distance between neighbouring grid points. To increase the available choice of mesh sizes, an initial trisection of the main triangles edges followed by bisections may be performed. The resulting grids are summarised in Tab. 1b.

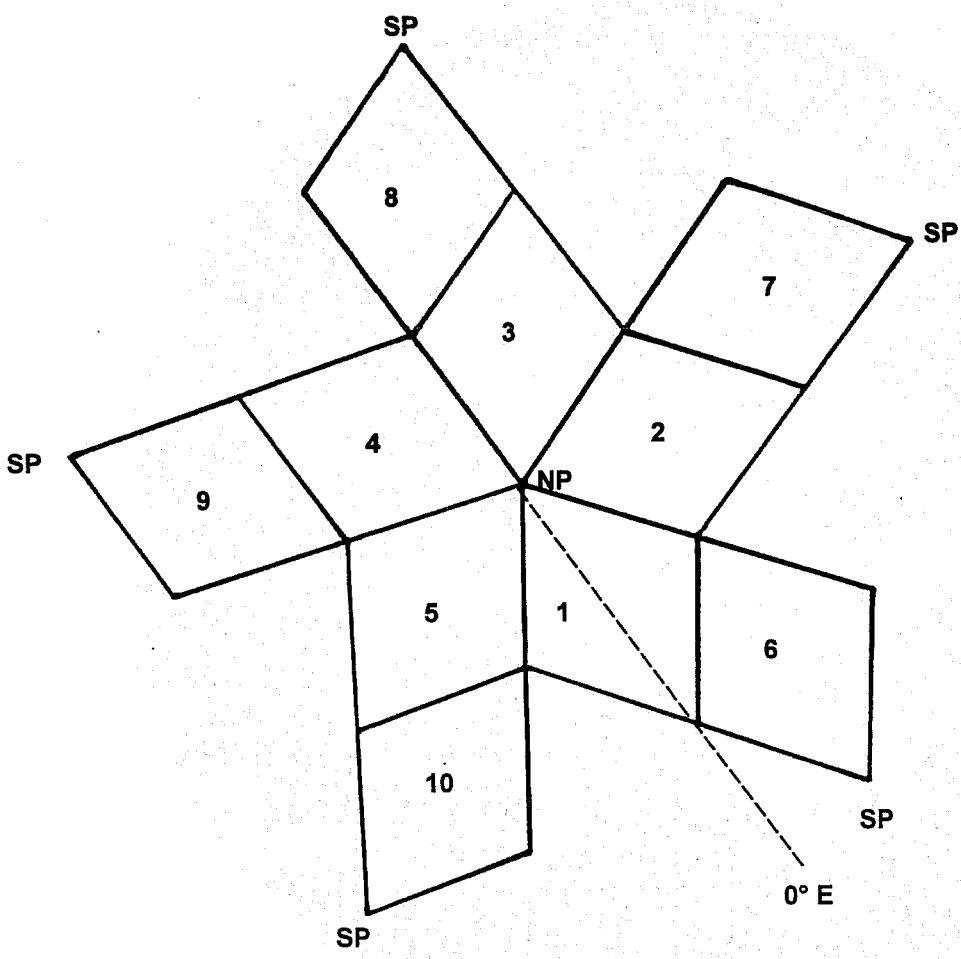

Figure 4 Logical data layout of the icosahedral-hexagonal grid of GME consisting of ten rhombi (diamonds), five containing the north pole and five the south pole.

By combining the $(ni+1)^2$ gridpoints of two adjacent major spherical triangles in a square matrix (Fig. 4), the global grid can logically also be viewed as the composition of ten rhombi (diamonds). Five diamonds contain the north pole and five the south pole. The data indexing (Fig. 5) is based on the convention that those ni^2 gridpoints which are only in *one* diamond are numbered from *1* to *ni* in the rows and columns of the data matrix. The points on the diamonds edges, *(0,1)* to *(0,ni+1)* and *(0,ni+1)* to *(ni,ni+1)*, are shared between

several diamonds and have to be exchanged each time step. The polar points *(0,1)* are even shared by five diamonds, namely diamond 1 to 5 share the north pole, diamonds 6 to 10 share the south pole.

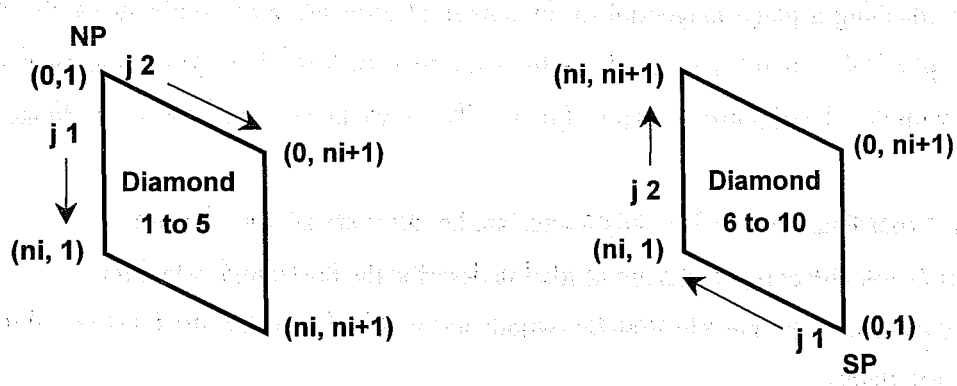

Figure 5 Indexing the gridpoints within one diamond; on the left for diamonds 1 to 5 which originate at the north pole, on the right for diamonds 6 to 10 which originate at the south pole.

From the computational point of view the icosahedral-hexagonal grid offers the additional advantage that no indirect addressing is required but the six (five) surrounding gridpoints can be accessed directly via pre-defined fixed stencils. Compared to unstructured grids a gain in the speed of computation by a factor of two or more can be realized due to the regular data storage.

Table 1 Some characteristic quantities of the icosahedral-hexagonal grid at different resolutions defined by *ni*, the number of intervals on a major triangle edge.
Here, $ngp = 10\ ni^2 + 2$ is the number of gridpoints, A_{min} is the minimum area of the hexagons, A_{max} is the maximum area of the hexagons; Δ_{av} is the average distance between gridpoints (= vertices of the triangles); Δ_{min} is the minimum distance between gridpoints; Δ_{max} is the maximum distance between gridpoints.

Table 1a Only bisections of major triangle edges, i.e. $ni = 2^k$, where k is a positive integer.

Ni	ngp	A_{min} (km^2)	A_{max} (km^2)	Δ_{av} (km)	Δ_{min} (km)	Δ_{max} (km)
16	2562	154109	238061	477.6	440.5	526.0
32	10242	38515	59955	239.3	220.3	263.2
64	40962	9628	15017	119.8	110.1	131.6
128	163842	2407	3756	59.9	55.1	65.8

Table 1b Initial trisection, followed by bisections of major triangle edges,
i.e. $ni = 3 * 2^k$, where k is a positive integer.

Ni	ngp	A_{min} (km^2)	A_{max} (km^2)	Δ_{av} (km)	Δ_{min} (km)	Δ_{max} (km)
24	5762	68477	97683	319.0	293.7	346.9
48	23042	17117	24494	159.7	146.8	173.5
96	92162	4279	6128	79.9	73.4	86.8
192	368642	1070	1532	40.0	36.7	43.4

3. DEFINITION OF THE FINITE-DIFFERENCE OPERATORS

The derivation of finite-difference operators is not based on Gauss´ theorem like in e.g. *Masuda and Ohnishi* (1987) but follows an approach which is closer to finite-element methods. A local spherical coordinate system is introduced by attaching a plane tangential to the sphere at each gridpoint (defined by the position vector $\mathbf{x}_0$). The local spherical system (η, χ) is defined by two unit vectors ($(\mathbf{e}_\lambda)_0$, $(\mathbf{e}_\varphi)_0$), one aligned with the global east, the other with the global north direction (Fig. 6). The advantages of this local coordinate system are

- within each cell the coordinate system is nearly Cartesian, i.e. there are no singularities,
- only two (tangential) velocity components are needed to describe the horizontal velocities.

However, there is one disadvantage, namely transformations are required between the local coordinate systems of neighbouring gridpoints.

The local spherical coordinates (η_m, χ_m) where m = 1,..,6 at hexagons and m = 1,...,5 at the twelve pentagons are used to determine the positions of the 6 (5) surrounding gridpoints relative to the central node, where $\eta = \chi = 0$, uniquely.

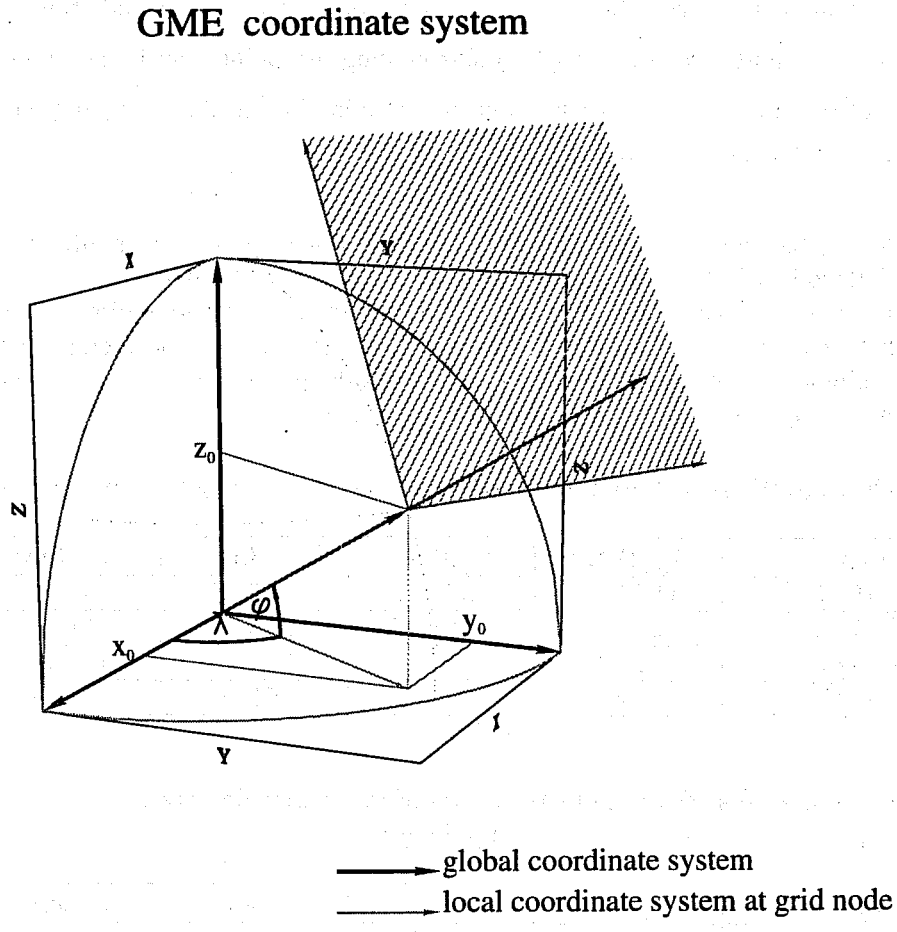

Figure 6 Global coordinate system (x, y, z) and local system (η, χ) at a gridpoint.

Because the meteorological equations are formulated and solved in the local spherical system (η, χ), based on the local Cartesian vectors $\mathbf{x}_0$, $(\mathbf{e}_\lambda)_0$, $(\mathbf{e}_\varphi)_0$, the usual operators have to be derived for this system.
The horizontal distances (*dx, dy*) on the earth of radius *a* are given by (3.1)

$$dx = a \cos\chi \, d\eta \qquad \text{and} \qquad dy = a \, d\chi \tag{3.1}$$

The analytical form of the operators follows from the usual form as given e.g. by *Dutton* (1976) taking into account that $\chi = 0$ at the central node, thus $cos\ \chi = 1$ and $sin\ \chi = 0$.

3.1 Definition of the gradient operator

The finite-difference form of the gradient operator for a scalar field ψ in the local coordinate system is written as a linear combination (Eqs. 3.2 and 3.3) involving the 6 (5) surrounding gridpoints and the central one. The numbering of the gridpoints is counterclockwise as shown in Fig. 7.

$$\frac{\partial \psi}{\partial \eta} = \sum_{m=1}^{6(5)} G_{\eta,m}(\psi_m - \psi_0) \tag{3.2}$$

$$\frac{\partial \psi}{\partial \chi} = \sum_{m=1}^{6(5)} G_{\chi,m}(\psi_m - \psi_0) \tag{3.3}$$

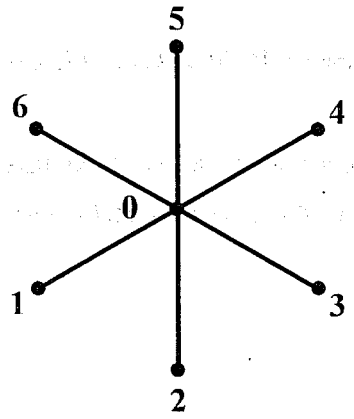

Figure 7 The central node (*0*) and the 6 surrounding neighbours (*1 to 6*) of a hexagon used by the elementary stencil of the icosahedral-hexagonal grid.

The coefficients $G_{\eta,m}$, $G_{\chi,m}$ (m = 1,...,6 (5)) are associated with the neighbouring nodes and depend only on the relative positions of the nodes described by the local coordinates (η, χ). ψ is an arbitrary scalar function of the local coordinates (η, χ). To calculate the coefficients $G_{\eta,m}$, $G_{\chi,m}$ the function ψ is represented locally as a quadratic polynomial ψ^* in the local coordinates (η, χ).

$$\psi^*(\eta,\chi) = \psi_0 + \alpha_1\eta + \alpha_2\chi + \alpha_3\eta^2 + \alpha_4\eta\chi + \alpha_5\chi^2 \tag{3.4}$$

For the case of six nearest neighbours at the hexagons, there are six constraints (m = 1,...,6) for the five coefficients α_1, α_2, ..., α_5, namely

$$\psi_m(\eta_m,\chi_m) = \psi_0 + \alpha_1\eta_m + \alpha_2\chi_m + \alpha_3\eta_m^2 + \alpha_4\eta_m\chi_m + \alpha_5\chi_m^2 \tag{3.5}$$

Eq. (3.5) may be interpreted as a Taylor series of the form

$$\psi_m(\eta_m,\chi_m) = \psi_0 + \left(\frac{\partial\psi}{\partial\eta}\right)_m \eta_m + \left(\frac{\partial\psi}{\partial\chi}\right)_m \chi_m + \frac{1}{2}\left(\frac{\partial^2\psi}{\partial\eta^2}\right)_m \eta_m^2 + \left(\frac{\partial\psi}{\partial\eta}\right)_m \left(\frac{\partial\psi}{\partial\chi}\right)_m \eta_m\chi_m + \frac{1}{2}\left(\frac{\partial^2\psi}{\partial\chi^2}\right)_m \chi_m^2 \tag{3.6}$$

A least squares procedure is used to solve for the five unknown coefficients

$$\alpha_j = \beta_{j,m}(\psi_m - \psi_0) \tag{3.7}$$

where j = 1,...,5, and the summation is over m = 1,...,6 (5).

Using Eqs. (3.2) through (3.7) the coefficients $G_{\eta,m}$, $G_{\chi,m}$ are then given by

$$G_{\eta,m} = \beta_{1,m} \quad \text{and} \quad G_{\chi,m} = \beta_{2,m} \tag{3.8}$$

where m = 1,...,6 (5).

Due to the intrinsic symmetry of the icosahedral-hexagonal grid the coefficients $G_{\eta,m}$, $G_{\chi,m}$ have to be computed only for diamond 1.

The definition of the flux divergence is based on the same coefficients but care has to be taken to rotate the wind components (u_m, v_m) of the surrounding six (five) nodes into the local spherical coordinate system of the central node (*0*).

3.2 Definition of the Laplace operator

Similar to the approach for the gradient operator, the Laplace operator is expressed in terms of the six (five) surrounding nodes.

$$\frac{\partial^2\psi}{\partial\eta^2} = \sum_{m=1}^{6(5)} L_{\eta,m}(\psi_m - \psi_0) \tag{3.9}$$

$$\frac{\partial^2\psi}{\partial\chi^2} = \sum_{m=1}^{6(5)} L_{\chi,m}(\psi_m - \psi_0) \tag{3.10}$$

The coefficients $L_{\eta,m}$, $L_{\chi,m}$ (m = 1,...,6 (5)) are associated with the neighbouring nodes and depend only on the relative positions of the nodes. The derivation of the coefficients $L_{\eta,m}$, $L_{\chi,m}$ closely follows the generation of the gradient operator. Using Eqs. (3.5), (3.6), (3.9) and (3.10) the coefficients $L_{\eta,m}$, $L_{\chi,m}$ are given by

$$L_{\eta,m} + L_{\chi,m} = 2\left(\beta_{3,m} + \beta_{5,m}\right) \tag{3.11}$$

Again, the coefficients have to be computed for diamond 1 only.

3.3 Interpolation in the icosahedral-hexagonal grid

Semi-Lagrangian advection schemes require the interpolation of fields from the icosahedral-hexagonal grid to the departure and midpoints of the parcel trajectory. Two types of interpolation schemes are considered here, namely *bilinear* and *biquadratic* ones. *Bilinear* interpolation is used during the calculation of the trajectory to derive the wind components (u, v) at the midpoint of the trajectory. *Biquadratic* interpolation is used to interpolate the prognostic fields to the departure point of the trajectory.

3.3.1 Bilinear interpolation

Bilinear interpolation of an arbitrary function $\psi(\eta,\chi)$ uses the values (ψ_0, ψ_m, ψ_{m-1}) at the three surrounding gridpoints (Fig. 8).

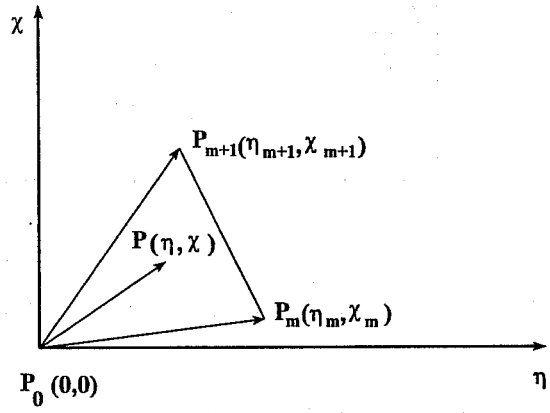

Figure 8 A triangle P_0, P_m, P_{m+1} in the local spherical (η,χ) coordinate system.

To derive the value $\psi(\eta,\chi)$ at point $P(\eta,\chi)$ barycentric coordinates are introduced. Each point within the triangle P_0, P_m, P_{m+1} (with the position vectors $\mathbf{p}_0$, $\mathbf{p}_m$, $\mathbf{p}_{m+1}$) is uniquely defined by the vector $\boldsymbol{p}$ where

$$\mathbf{p} = \gamma_0\mathbf{p}_0 + \gamma_1\mathbf{p}_m + \gamma_2\mathbf{p}_{m+1} \qquad \text{where} \quad \gamma_0 + \gamma_1 + \gamma_2 = 1 \tag{3.12}$$

$(\gamma_0, \gamma_1, \gamma_2)$ are called the barycentric coordinates of the point P. To calculate these coordinates the following linear system has to be solved (note that at the central node P_0: $\eta = \chi = 0$).

$$\eta = \gamma_1 \eta_m + \gamma_2 \eta_{m+1} \quad \text{and} \quad \chi = \gamma_1 \chi_m + \gamma_2 \chi_{m+1} \quad \text{and} \quad \gamma_0 = 1 - \gamma_1 - \gamma_2 \tag{3.13}$$

Thus the bilinear interpolation of $\psi(\eta,\chi)$ within the triangle P_0, P_m, P_{m+1} is given by

$$\psi(\eta,\chi) = \gamma_0 \psi(\eta_0,\chi_0) + \gamma_1 \psi(\eta_m,\chi_m) + \gamma_2 \psi(\eta_{m+1},\chi_{m+1}) \tag{3.14}$$

3.3.2 Biquadratic interpolation

The formula for the biquadratic interpolation is based on an Hermitian approach where the gradients of the function $\psi(\eta,\chi)$ at the vertices are used to define values of ψ at the midpoints of the triangle edges (Fig. 9).

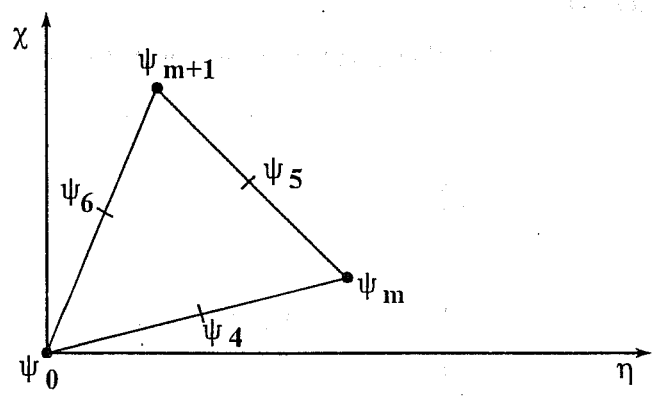

Figure 9 The six values used for the biquadratic interpolation of a function $\psi(\eta,\chi)$ in a triangle.

The standard biquadratic interpolation formula for a triangle in terms of values at the triangle vertices and midpoints of the edges is applied to obtain the value of ψ at an arbitrary point $P(\eta,\chi)$ in the triangle.

$$\begin{aligned}\psi(\gamma_0,\gamma_1,\gamma_2) = {} & \gamma_0(2\gamma_0 - 1)\psi_0 + \gamma_1(2\gamma_1 - 1)\psi_m + \gamma_2(2\gamma_2 - 1)\psi_{m+1} \\ & + 4(\gamma_0\gamma_1\psi_4 + \gamma_1\gamma_2\psi_5 + \gamma_2\gamma_0\psi_6)\end{aligned} \tag{3.15}$$

where $(\gamma_0, \gamma_1, \gamma_2)$ are the barycentric coordinates of the point P. The values of the function ψ at the midpoints of the triangle edges, i.e. ψ_4, ψ_5, ψ_6, are derived from the gradients at the given points P_0, P_m, P_{m+1}. Thus the biquadratic interpolation is based on a stencil which includes twelve gridpoints (Fig. 10).

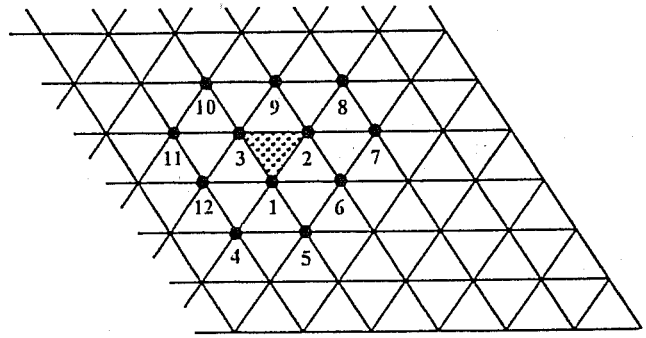

Figure 10 The twelve gridpoints involved in the biquadratic interpolation in the triangle P_0, P_m, P_{m+1}.

Monotonicity may be enforced by simply demanding that the interpolated value is not higher or lower than the values at the three corner points P_0, P_m, P_{m+1}. In the same way, *positive definiteness* may be enforced by the condition that the interpolated value is greater than or equal to 0. If the Courant numbers are restricted to values less than 1 it is fairly easy to determine which of the 6 (5) surrounding triangles contain the departure or midpoint of the trajectory. Without this restriction the search algorithm is more complicated and uses a binary search method to speed up convergence.

4. ACCURACY OF THE GRADIENT AND LAPLACE OPERATORS

Heikes and Randall (1995b) introduced the following function to test the accuracy of their finite-difference operators on the icosahedral-hexagonal grid

$$\beta_{m,n}(\lambda,\varphi) = a^2 \cos(m\lambda)\cos^4(n\varphi) \tag{4.1}$$

where λ is the longitude, φ is the latitude, a is the radius of the earth, and m, n are integers set to 1 or 3. For different resolutions ni of the grid mesh the analytical solution x^{true} is compared to the finite-difference one x^{fd}, and some error norms are evaluated. The *one-norm* is defined by

$$\left\| x^{fd} - x^{true} \right\|_1 = \frac{1}{A}\sum_{i=1}^{N} A_i \left| x_i^{fd} - x_i^{true} \right| \tag{4.2}$$

where the summation is over all N gridpoints of the icosahedral-hexagonal grid, and

$$A = \sum_{i=1}^{N} A_i \tag{4.3}$$

is the area of the globe, A_i is the area of a particular hexagon (pentagon).

The *two-norm* is defined by

$$\left\| x^{fd} - x^{true} \right\|_2 = \left[\frac{1}{A} \sum_{i=1}^{N} A_i \left(x_i^{fd} - x_i^{true} \right)^2 \right]^{1/2} \tag{4.4}$$

and the infinity norm is defined by

$$\left\| x^{fd} - x^{true} \right\|_\infty = \max\left(\left| x_i^{fd} - x_i^{true} \right|, i = 1, N \right) \tag{4.5}$$

A finite-difference operator will not be *consistent* if the infinity norm does not converge to 0 for decreasing mesh sizes. Figs. 11 to 13 summarize the results for the gradient and Laplace operators of GME defined in section 3. Both operators fulfil the consistency requirement, and their general accuracy is second order because the error norms drop roughly by a factor of *4* if the resolution *ni* is doubled. Thus the operators used in GME on the simple icosahedral-hexagonal grid show an accuracy which is similar to the one of the operators derived by *Heikes and Randall* (1995 b, see Fig. 4 there) on the improved twisted icosahedral-hexagonal grid where some optimization of the gridpoint distribution has been performed additionally.

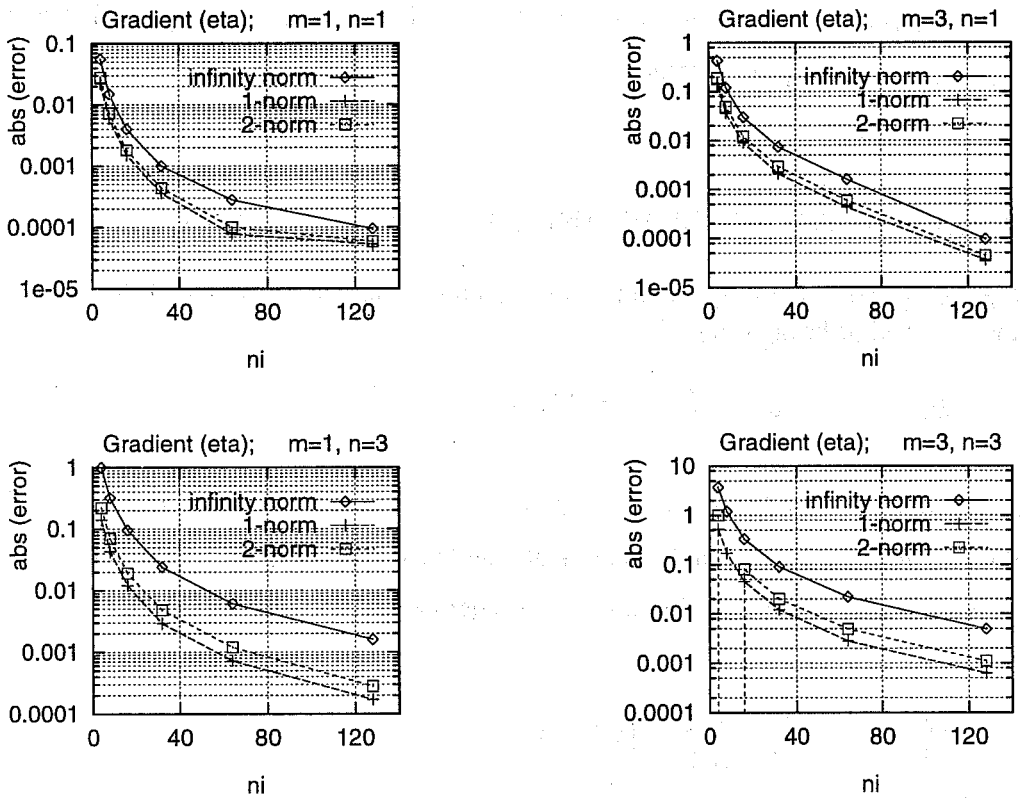

Figure 11 Error in the finite-difference gradient operator (zonal direction) for the test function proposed by *Heikes and Randall* (1995 b) for different values of *m* and *n*. Parameter *ni* describes the resolution.

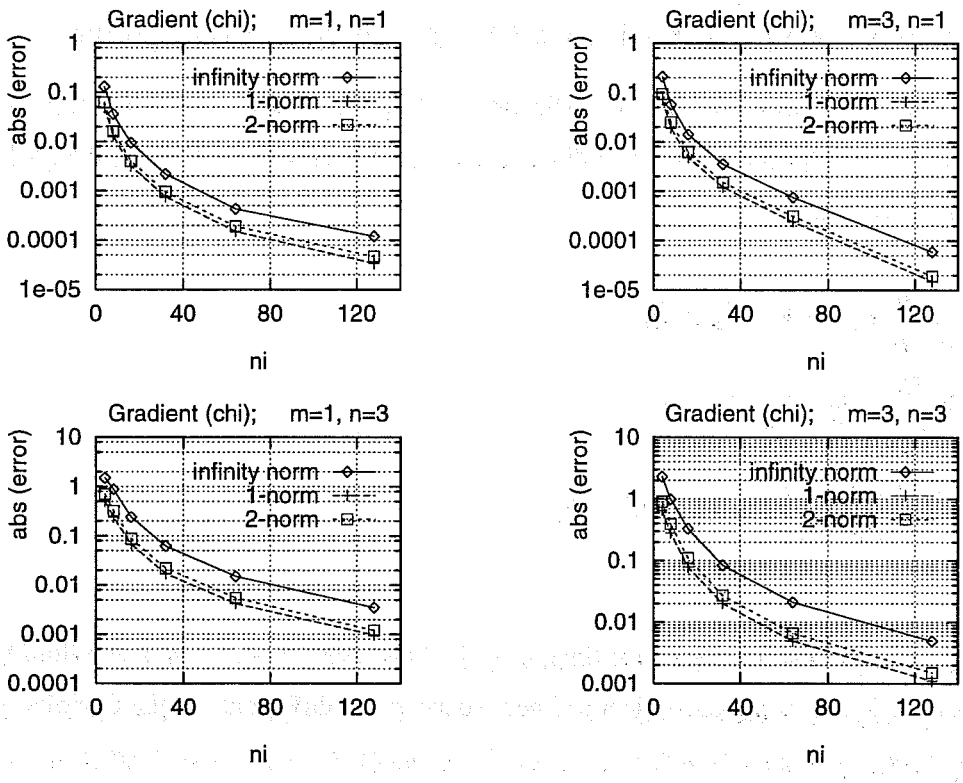

Figure 12 Same as Figure 11 but meridional direction of gradient operator.

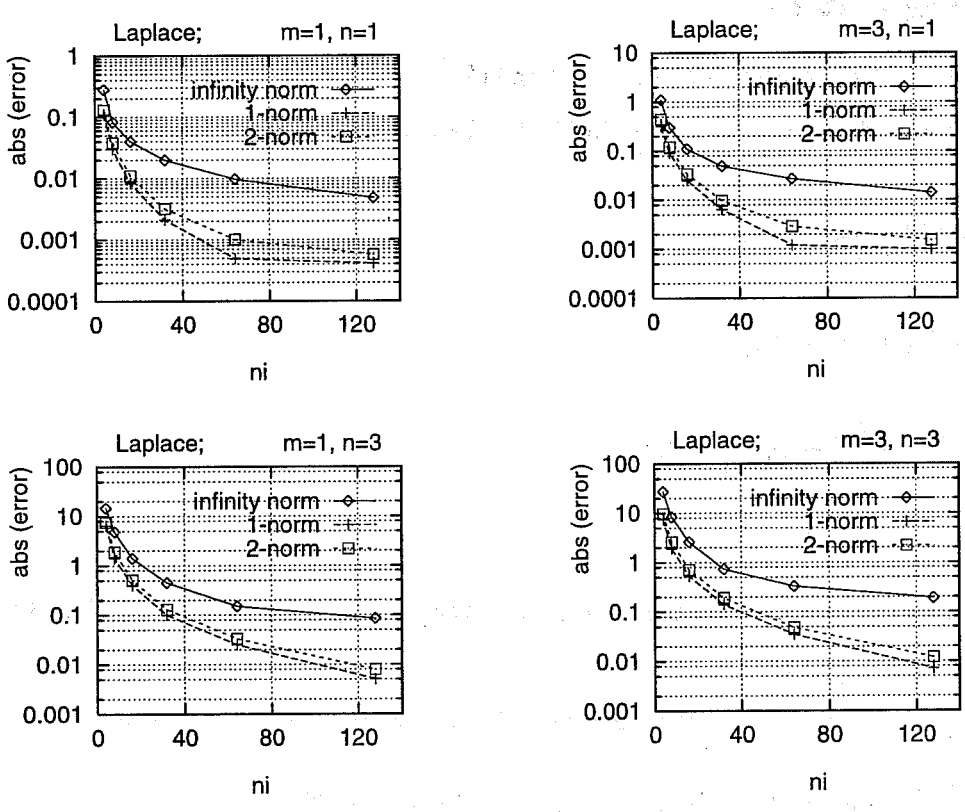

Figure 13 Error in the finite-difference Laplace operator for the test function proposed by *Heikes and Randall* (1995 b) for different values of *m* and *n*. Parameter *ni* describes the resolution.

5. SHALLOW WATER VERSION OF GME AND RESULTS OF TEST CASES

A well-established test bed for new discretization schemes is the shallow water test suite proposed by *Williamson et al.* (1992). For the local spherical coordinate system (η,χ) outlined in section 3 the shallow water equations take the following form

$$\frac{du}{dt} = -\frac{g}{a}\frac{\partial h}{\partial \eta} + fv - K_4\nabla^4 u = R_u \tag{5.1}$$

$$\frac{dv}{dt} = -\frac{g}{a}\frac{\partial h}{\partial \chi} - fu - K_4\nabla^4 v = R_v \tag{5.2}$$

$$\frac{dh^*}{dt} = -\frac{h^*}{a}\left(\frac{\partial u}{\partial \eta} + \frac{\partial v}{\partial \chi}\right) - K_4\nabla^4 h^* = R_h \tag{5.3}$$

where

u,v are zonal (meridional) wind components; t is time; h^* is the fluid depth; $h = h^* + h_s$ is the fluid height and h_s is the surface topography; K_4 is the coefficient of linear fourth order diffusion; f is the Coriolis parameter; a is the radius of the earth; g is the constant of gravity; R_u, R_v, R_h are the right-hand sides of the prognostic equations.

5.1 Semi-Lagrangian scheme

The explicit semi-Lagrangian solution of (5.1), (5.2) and (5.3) for a three-time-level scheme where n-1, n, n+1 are defining the time levels for t-Δt, t, t+Δt can be formally written as

$$u^{n+1} = I_d\left\{u^{n-1}\right\} + 2\Delta t\, I_m\left\{R_u\right\} \tag{5.4}$$

$$v^{n+1} = I_d\left\{v^{n-1}\right\} + 2\Delta t\, I_m\left\{R_v\right\} \tag{5.5}$$

$$\left(h^*\right)^{n+1} = I_d\left\{\left(h^*\right)^{n-1}\right\} + 2\Delta t\, I_m\left\{R_h\right\} \tag{5.6}$$

where

I_d denotes the horizontal interpolation of the prognostic variables at the previous time level (t-Δt) to the departure point of the trajectory, and

I_m denotes the horizontal interpolation of the right-hand sides to the midpoint of the trajectory.

Departure and midpoints are found by the usual iterative two-step procedure.

5.2 Explicit Eulerian scheme

The explicit Eulerian solution of (5.1), (5.2) and (5.3) takes the following form

$$u^{n+1} = u^{n-1} + 2\Delta t\left[\left(\varsigma^n + f\right)v^n - \frac{1}{a}\frac{\partial}{\partial \eta}\left(gh^n + K^n\right) - K_4\nabla^4 u^{n-1} \right] \tag{5.7}$$

$$v^{n+1} = v^{n-1} + 2\Delta t\left[-\left(\varsigma^n + f\right)u^n - \frac{1}{a}\frac{\partial}{\partial \chi}\left(gh^n + K^n\right) - K_4\nabla^4 v^{n-1} \right] \tag{5.8}$$

$$\left(h^*\right)^{n+1} = \left(h^*\right)^{n-1} + 2\Delta t\left[-\frac{u^n}{a}\frac{\partial\left(h^*\right)^n}{\partial \eta} - \frac{v^n}{a}\frac{\partial\left(h^*\right)^n}{\partial \chi} - \frac{\left(h^*\right)^n}{a}\left(\frac{\partial u^n}{\partial \eta} + \frac{\partial v^n}{\partial \chi}\right) - K_4\nabla^4\left(h^*\right)^{n-1} \right] \tag{5.9}$$

where

$\varsigma = \frac{1}{a}\left(\frac{\partial v}{\partial \eta} - \frac{\partial u}{\partial \chi}\right)$ is the vorticity and $K = \frac{1}{2}\left(u^2 + v^2\right)$ is the specific kinetic energy.

5.3 Semi-implicit scheme

Because explicit schemes are not very efficient due to the short time steps required to fulfil the CFL criterion, a semi-implicit treatment of the gravity wave terms is derived following *Robert* (1981). A slight off-centering is necessary to stabilize the semi-implicit solution, i.e. the temporal average of a variable ψ (where $\psi = u, v, h^*$) is written as

$$\overline{\psi} = \alpha\psi^{n+1} + (1-\alpha)\psi^{n-1} \tag{5.10}$$

Setting the weight α of the new time level to a value greater than 0.5 results in a damping of the gravity waves; α is set to 0.7. The usual two-dimensional Helmholtz equation (modified by α) for the second temporal derivative of the deviation of the height field from the mean state is solved by a simple successive overrelaxtion method (SOR), a faster multi-grid method based on *Baumgardner and Frederiksen* (1985) can be used, too.

The semi-implicit time step is about a factor of 5 to 6 larger than the explicit one and allows an efficient solution of the shallow water equations. But the current semi-implicit, semi-Lagrangian version of the program is restricted to Courant numbers less than 1 because search algorithm and communication pattern in the ico-

sahedral-hexagonal grid become very complex if the parcel trajectory departs outside the six (five) surrounding triangles.

5.4 Results for test cases 5 and 6 of the Williamson et al. (1992) test suite

Test case 5 consists of a zonal flow impinging on a mountain of a maximum height of 2000 m. No analytical solution exists but a spectral T106 simulation is taken as reference. To ease the comparison between GME and the spectral reference, the spectrally fitted mountain (including the *spectral ringing*) is interpolated to the icosahedral-hexagonal grid. For GME, the semi-implicit, semi-Lagrangian version at a resolution $ni = 64$ (mesh size ~ 120 km) has been taken. The solutions of both models at day 10 (Fig. 14) and day 20 (not shown) agree very well.

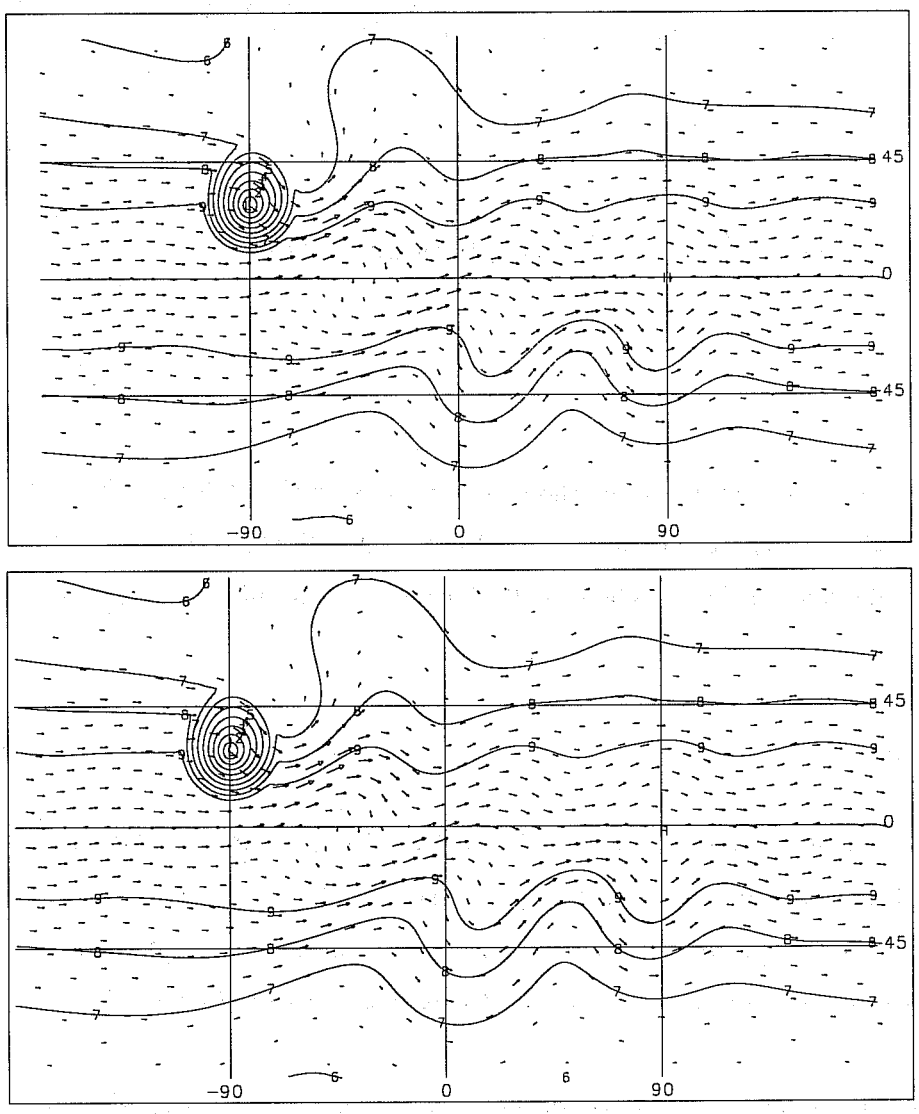

Contour values (m) :

2 - 4200
4 - 4640
6 - 5080
8 - 5520

Max. velocity: 42 m/s

Figure 14 Results of test case 5 at day 10.
Top: Spectral reference model at T106,
bottom: Semi-implicit, semi-Lagrangian version of GME at resolution ni = 64 (Δ ~ 120 km).

The initial condition for test case 6 is a wavenumber 4 Rossby-Haurwitz wave which is not an analytical solution for the shallow water model. Here again, the spectral T106 model serves as the reference. Fig. 15 compares three versions of the icosahedral-hexagonal gridpoint model to the spectral reference (Fig. 15a) at day 10, the semi-implicit, semi-Lagrangian version at resolution *ni* = 64 (Fig. 15b), the semi-implicit Eulerian version at the same resolution (Fig. 15c), and the same model version at resolution *ni* = 128 (Fig. 15d). Again, the GME matches the spectral reference very well. But a slight tendency to develop asymmetries between the hemispheres in spite of the symmetric initial condition is visible at resolution *ni* = 64. On the other hand, no *wavenumber-five problem* can be detected. This problem was common in the first icosahedral-hexagonal models, and was caused by an interaction of the flow with the grid due to the distortion of the grid boxes close to the twelve special points.

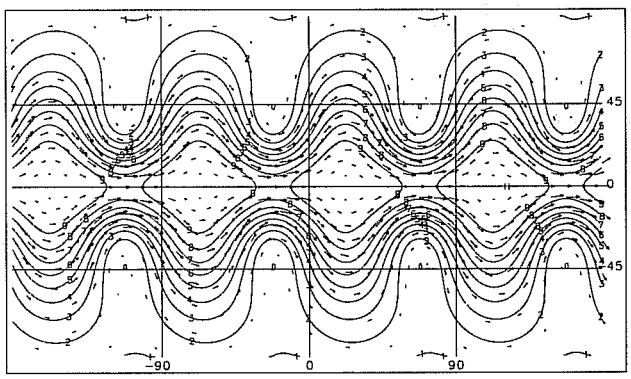

a)Contour values (m) :
2 – 8650 4 – 9120
6 – 9590 8 – 10060

Max. velocity: 97 m/s

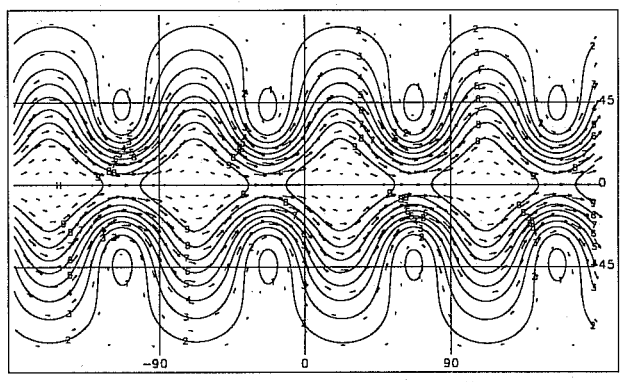

b)Contour values (m) :
2 – 8650 4 – 9140
6 – 9600 8 – 10060

Max. velocity: 97 m/s

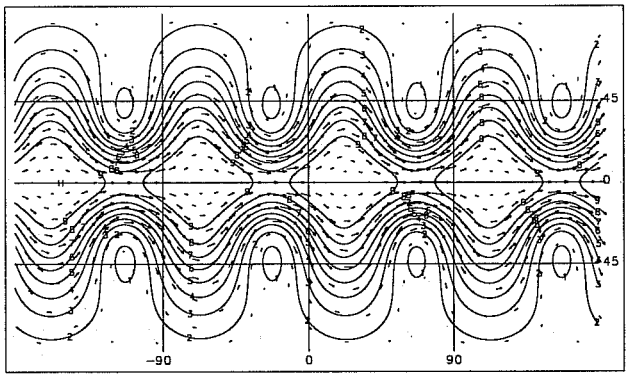

c)Contour values (m) :
2 – 8680 4 – 9140
6 – 9600 8 – 10060

Max. velocity: 97 m/s

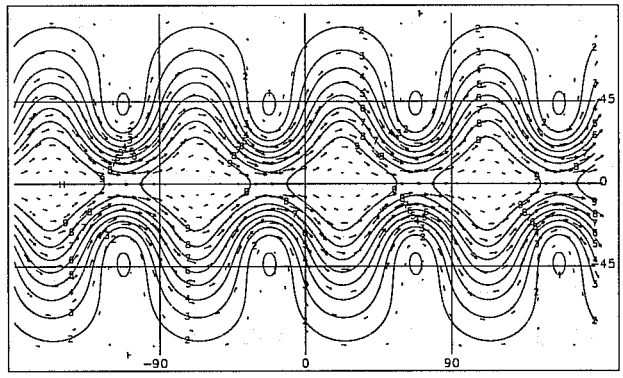

d)Contour values (m) :
2 – 8670 4 – 9140
6 – 9610 8 – 10080

Max. velocity: 97 m/s

Figure 15 Results of test case 6 at day 10.
a) Spectral reference model at T106,
b) Semi-implicit, semi-Lagrangian version of GME at resolution ni = 64 ($\Delta \sim 120$ km),
c) Semi-implicit, Eulerian version of GME at resolution ni = 64 ($\Delta \sim 120$ km),
d) Semi-implicit, Eulerian version of GME at resolution ni = 128 ($\Delta \sim 60$ km).

6. THREE-DIMENSIONAL VERSION OF GME

6.1 Differential form of model equations

The encouraging results obtained by the shallow water version of GME prompted the development of the three-dimensional version of the model. The prognostic equations are written in differential form for local spherical coordinates (η,χ) and a hybrid vertical coordinate ξ.

$$\frac{\partial u}{\partial t}-(\varsigma+f)v+\dot{\xi}\frac{\partial u}{\partial \xi}=-\frac{1}{a}\frac{\partial}{\partial \eta}(\Phi+K)-\frac{RT_v}{a}\frac{\partial}{\partial \eta}(\ln p)+\left(\frac{\partial u}{\partial t}\right)_{sub}-K_4\nabla^4 u \tag{6.1}$$

$$\frac{\partial v}{\partial t}+(\varsigma+f)u+\dot{\xi}\frac{\partial v}{\partial \xi}=-\frac{1}{a}\frac{\partial}{\partial \chi}(\Phi+K)-\frac{RT_v}{a}\frac{\partial}{\partial \chi}(\ln p)+\left(\frac{\partial v}{\partial t}\right)_{sub}-K_4\nabla^4 v \tag{6.2}$$

$$\frac{\partial T}{\partial t}+\frac{u}{a}\frac{\partial T}{\partial \eta}+\frac{v}{a}\frac{\partial T}{\partial \chi}+\dot{\xi}\frac{\partial T}{\partial \xi}=\frac{\alpha\omega}{c_p}+\frac{L_v}{c_p}C_{vl}+\left(\frac{\partial T}{\partial t}\right)_{sub}-K_4\nabla^4(T-T_{ref}) \tag{6.3}$$

$$\frac{\partial p_s}{\partial t}=-\frac{1}{a}\int_0^1\left\{\frac{\partial}{\partial \eta}\left(u\frac{\partial p}{\partial \xi}\right)+\frac{\partial}{\partial \chi}\left(\frac{\partial p}{\partial \xi}\right)\right\}d\xi \tag{6.4}$$

$$\frac{\partial q_v}{\partial t}+\frac{u}{a}\frac{\partial q_v}{\partial \eta}+\frac{v}{a}\frac{\partial q_v}{\partial \chi}+\dot{\xi}\frac{\partial q_v}{\partial \xi}=-C_{vl}+\left(\frac{\partial q_v}{\partial t}\right)_{sub}-K_4\nabla^4 q_v \tag{6.5}$$

$$\frac{\partial q_l}{\partial t}+\frac{u}{a}\frac{\partial q_l}{\partial \eta}+\frac{v}{a}\frac{\partial q_l}{\partial \chi}+\dot{\xi}\frac{\partial q_l}{\partial \xi}=C_{vl}+\left(\frac{\partial q_l}{\partial t}\right)_{sub} \tag{6.6}$$

where

u,v are the zonal (meridional) wind components; T is the temperature; p_s is the surface pressure; q_v is the specific water vapour content, q_l is the specific cloud liquid water content; ζ is the vorticity and K the specific kinetic energy; p is the pressure, T_v is the virtual temperature; T_{ref} is a reference temperature depending only on height; C_{vl} is the condensation rate; $(..)_{sub}$ is the sub-grid scale tendency due to parameterized processes like radiation, convection or turbulence.

6.2 Numerical solution of the three-dimensional equation set

The semi-Lagrangian and the Eulerian versions of the shallow water model of GME produce very similar results but the Eulerian code is about 20% faster. Therefore, the *dry* part of the three-dimensional version of GME, i.e. the prognostic equations for u, v, T, p_s, *is* solved by the semi-implicit Eulerian method, and only the two prognostic moisture equations (q_v, q_l) use semi-Lagrangian advection in the horizontal direction to

allow for monotonicity and positive definiteness. In the vertical, the energy and angular momentum conserving finite-difference scheme of *Simmons and Burridge* (1981) is applied to all prognostic equations.
The semi-implicit treatment of gravity waves leads to a three-dimensional Helmholtz equation for the second temporal derivative of the divergence of the horizontal wind field. The eigenvectors of the vertical structure matrix are used to diagonalize this 3-d equation into *i3e* 2-d Helmholtz equations where *i3e* is the number of layers in the model. Currently, these 2-d equations are solved by successive overrelaxation. Again, slight off-centering of the implicit terms is necessary to damp the gravity waves and to stabilize the solution. Part of the sub-grid scale tendencies are treated implicitly for stability reasons, too.

6.3 Physical parameterizations

Since GME will replace GM and EM most physical parameterizations have been taken from the regional model EM. Thus the current physical package of GME consists of

- radiation scheme (*Ritter and Geleyn,* 1992); a full radiation step is performed every two hours,
- grid-scale precipitation scheme including parameterized cloud microphysics,
- moist convection (*Tiedtke,* 1989),
- vertical turbulent fluxes; in the Prandtl-layer based on *Louis* (1979), for the boundary layer and the free atmosphere a level-two scheme according to *Mellor and Yamada* (1974),
- sub-grid scale orographic effects (*Lott and Miller,* 1997),
- soil model (*Jacobsen and Heise,* 1982),
- cloudiness derived from specific cloud liquid water content, relative humidity, convective activity and stability.

To save computing time, part of the parameterization schemes (convection, turbulent fluxes, sub-grid scale orographic effects) are called only every fifth time step of the model.
Some of these schemes have been used operationally only in the European domain of EM; a fine-tuning for global use will be necessary but has not been performed so far. In spite of this, first results of integrations of the full model over a whole month (see section 8) have been encouraging.

6.4 Digital filtering initialization

Initialization schemes have to remove noise from the forecast while causing acceptable small changes to the analysis and forecasts. In addition, it is an advantage if the initial spin-up of the model is reduced because a balance between humidity and dynamic fields has been achieved during initialization. For GME, the digital filtering initialization of Lynch (1997), involving a 3-h adiabatic backward integration and a 3-h diabatic forward one centered around the initial time, has been implemented.

7. TEST OF THE DYNAMICAL CORE OF GME

The dynamical core of GME has been investigated using a proposal of *Held and Suarez* (1994). The idea behind this test is to substitute the physics package with simplified physics. The forcing consists of a temperature relaxation and Rayleigh friction for the wind in lower layers. The analysis of the dynamical core of GME is concentrated on an inspection of convergence with resolution, of symmetry aspects, and on a comparison to the spectral model GM. All GM and GME experiments – using a vertical resolution of 19 unequally spaced hybrid layers – are started from a dry isothermal state at rest without topography. The experiments cover a period of 1200 days. The first 200 days are omitted in the computation of the model climate. Fig. 16 taken from *Jablonowski* (1998) presents the time-mean (day 200 to 1200) zonal mean of the zonal wind for different resolutions of GME. The patterns look similar concerning the overall structures and strength of the jet streams. Some differences occur in the wind fields in upper levels and in the position of the jets. The symmetry of the pattern with respect to the equator improves with finer resolution.

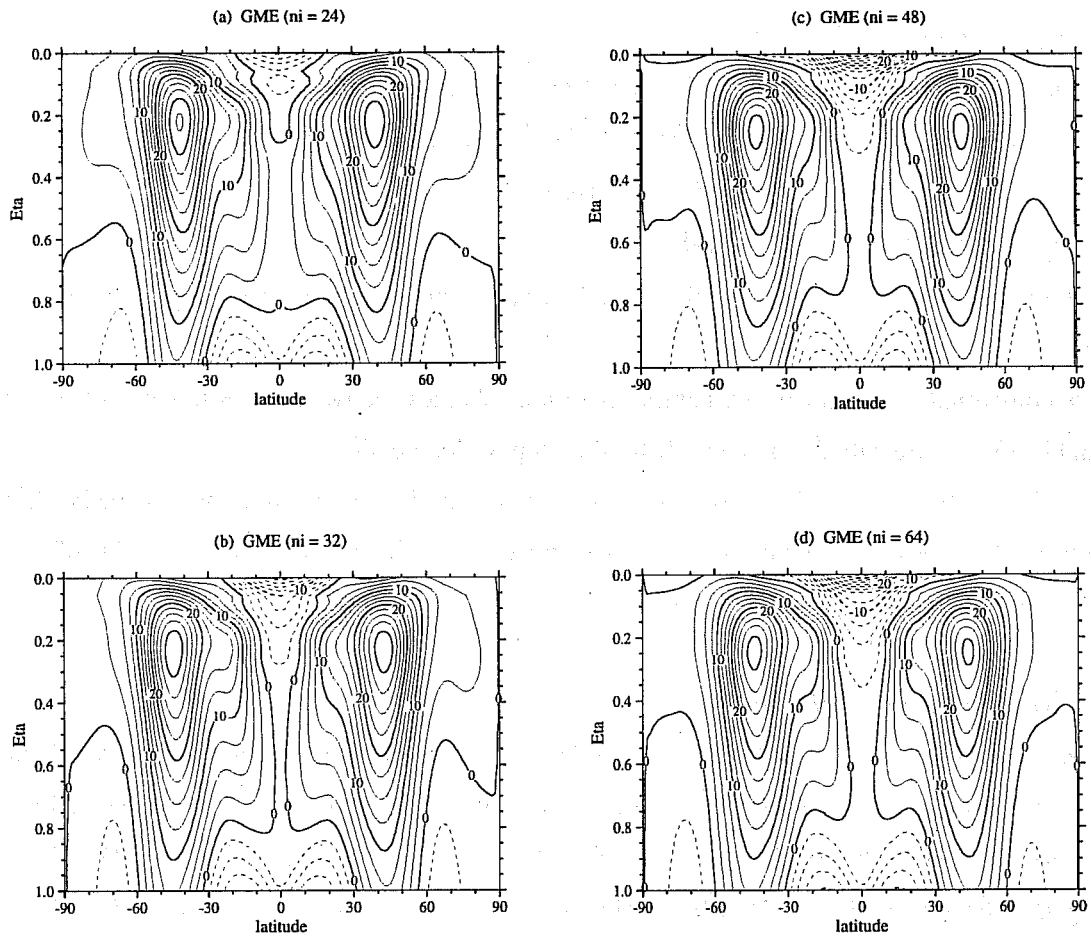

Figure 16 Zonal mean, time-mean (day 200 to 1200) of zonal wind u (m/s) for different resolutions *ni* of GME.

Comparing the spectral GM at resolution T106 and GME at *ni* = 64 indicates good correspondence even for derived quantities like the vertical eddy temperature transport (Fig. 17 a) or the meridional eddy temperature transport (Fig. 17 b).

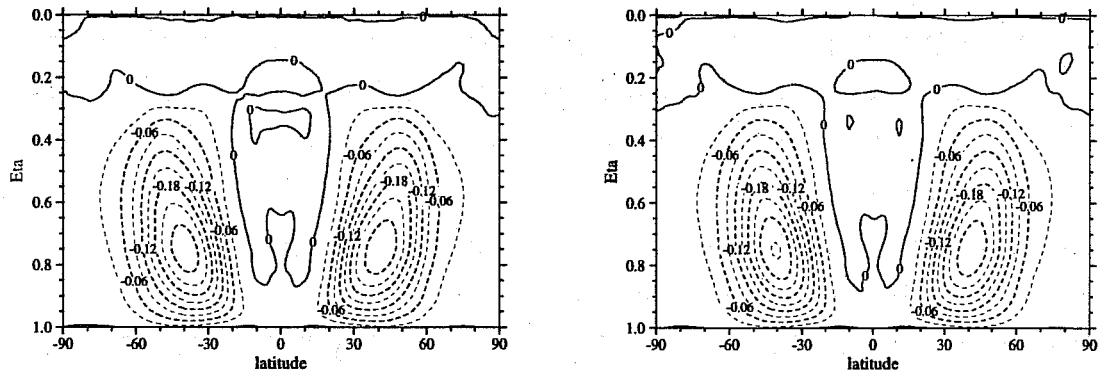

Figure 17 a) **Zonal mean, time-mean (day 200 to 1200) of the vertical eddy temperature transport (K Pa/s).**
Left: GM (resolution T106), right: GME (resolution *ni* = 64)

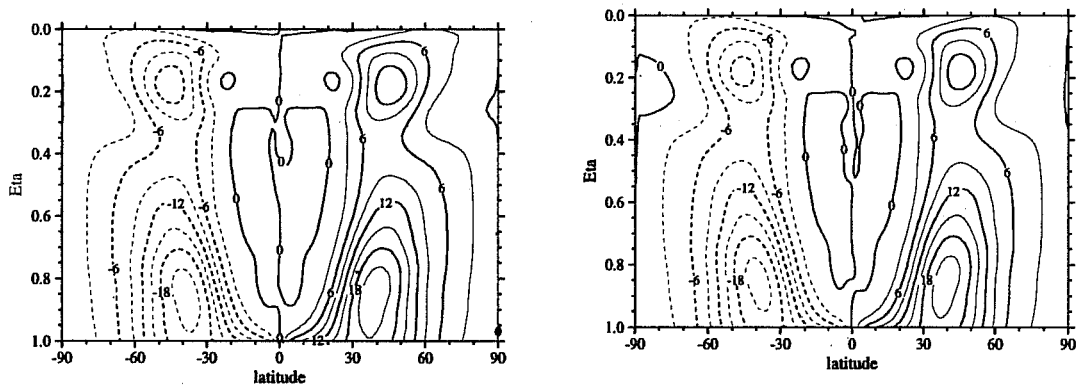

Figure 17 b) Zonal mean, time-mean (day 200 to 1200) of the meridional eddy temperature transport (K m/s).
Left: GM (resolution T106), right: GME (resolution *ni* = 64)

8. FIRST RESULTS OF THE FULL THREE-DIMENSIONAL VERSION OF GME

8.1 Some computational aspects of GME

Since the design of GME included a domain decomposition from the beginning, it took only three months to parallelize the program using MPI (Message Passing Interface) for message passing. The code is written in standard FORTRAN 90 and fully portable. For the two-dimensional domain decomposition the $(ni+1)^2$ grid-points of each diamond are divided among *n1 x n2* processing elements (PEs). Thus each PE computes the forecast in a subdomain of *all ten* diamonds. Because of this there is a better chance to achieve some load balancing for the physical parameterizations, e.g. between day/night, land/sea or rain/no rain. For example, on 13 x 13 PEs of a Cray T3E1200 the physical parameterizations for a 24-h real data forecast consume between 231s and 288s of wallclock time; the average time is 259s. In the current version of GME, each computational subdomain has a *halo* of just two rows and columns of gridpoints around which have to be exchanged via MPI with those PEs which compute the forecast in the neighbouring subdomains. There are only seven synchronization points during one complete forecast step.

Fig. 18 shows the speed-up of GME (*ni* = 128, 31 layers) on a Cray T3E1200 for a 24-h real data forecast without writing GRIB files. Between 5 x 5 and 13 x 13 PEs an almost linear speed-up can be realised. About 9 x 9 PEs are necessary to perform a 24-h forecast in less than 24 minutes at a sustained speed of about 69 MFlops/PE, roughly 5.5 GFlops for the whole model.

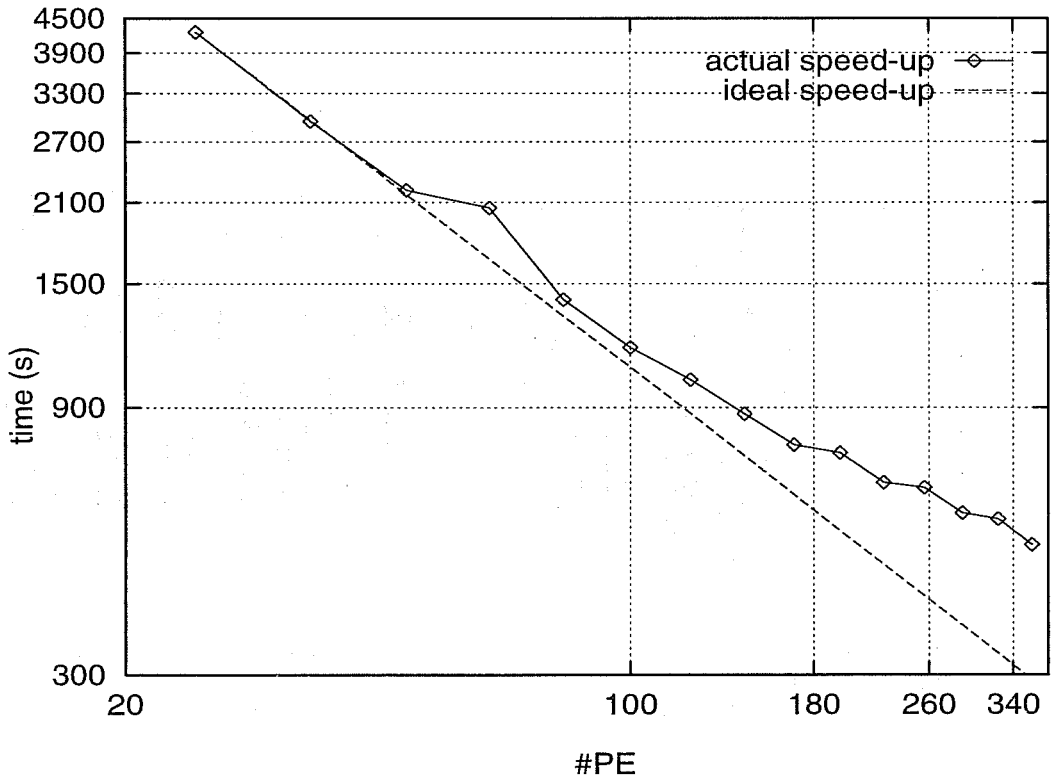

Figure 18 Speed-up of GME (*ni* = 128, 31 layers) on a Cray T3E1200 for a 24-h real data forecast without writing GRIB files.

The distribution of the cost of the different parts of GME expressed as percentage of the total floating point operations (Flop, left) and as percentage of the total wallclock time (right) is highlighted in Fig. 19. The solution of the Helmholtz equations by the relatively slow SOR method takes only 2% of the total number of Flop but about 17% of the time. Clearly, some optimization of the code is possible and will take place in the near future.

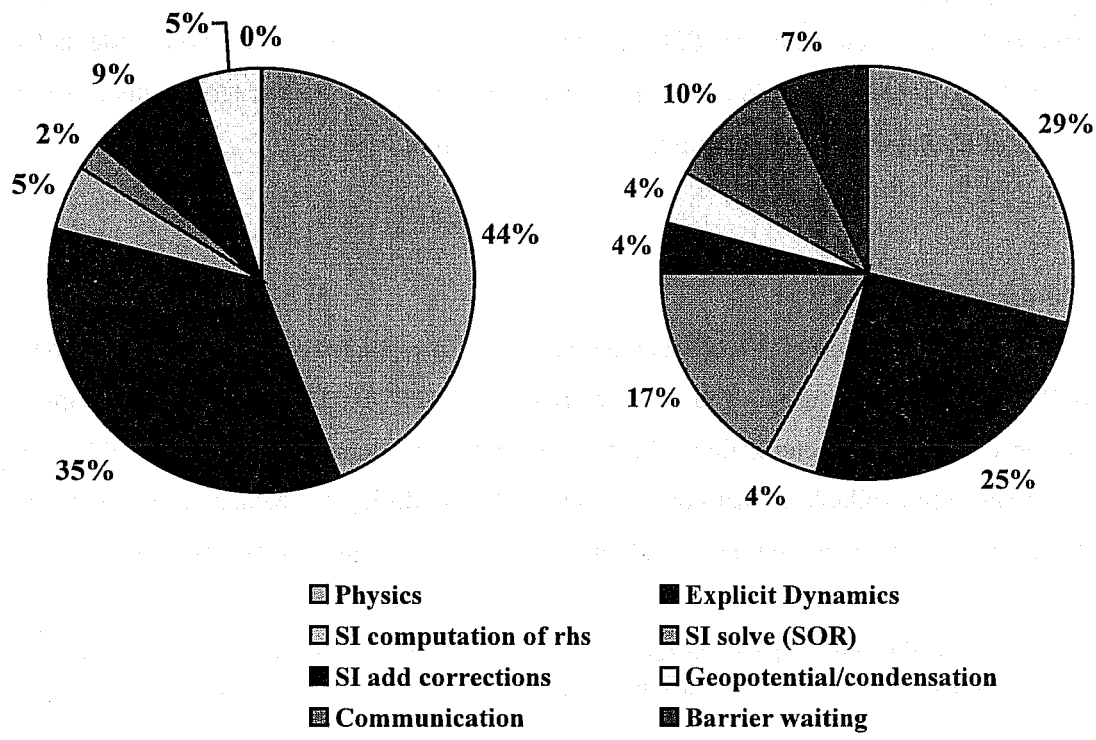

Figure 19 Cost of the different parts of GME (*ni* = 128, 31 layers) on a Cray T3E1200 for a 24-h real data forecast without writing GRIB files. 13 x 13 PEs have been used.
Left: Cost expressed as percentage of the total floating point operations (Flop).
Right: Cost expressed as percentage of the total wallclock time.

Table 2 Comparison of some characteristic numbers of three global models in Europe.

Model	Number of points/ layer	Number of Layers	Average mesh size (km)	Cost of 24-h forecast (no output)
GME (DWD)	163842	31	59.9	7.2 TFlop
IFS (ECMWF)	138346	31	62.5	4.9 TFlop
UM (UKMO)	140400	30	61.5	4.8 TFlop

Tab. 2 compares GME with the IFS (ECMWF) and UM (UK Met. Office) from the computational point of view. The cost of the models are expressed in number of floating point operations for a 24-h forecast with-

out GRIB output (for UM including I/O). Compared to IFS and UM the cost of GME seems to be much higher, but after adjusting for the larger number of gridpoints and the smaller mesh size GME is only about 18% more expensive. At higher resolutions, e.g. for GME with $ni = 256$ ($\Delta \sim 30$ km) and IFS with T_L639, the cost of a 24-h forecast is about the same for both models, namely 44 TFlop. Beyond this resolution, GME will be less expensive because the cost of the Legendre transform will dominate IFS. On the other hand, efficiency cannot be measured by these simple numbers but require detailed evaluation of issues like single-node performance on vector or RISC architectures, possible speed-up on MPP systems, and the multitasking overhead. Finally, forecast quality is probably the most important criterion which requires a steady improvement of data assimilation, modelling, and postprocessing.

8.2 30-day experiments

A first test of GME consisted of 30-day runs initialized by interpolated GM analysis. A resolution of $ni = 128$ and 31 layers have been used. Tab. 3 summarizes the results for December 1992. Despite the lack of tuning of the physical parameterization schemes the simulated globally averaged variables are mostly in good agreement with available climatological values. The hydrological balance is maintained rather well with a 30-day average precipitation rate of 2.94 mm/d and a corresponding evaporation of 2.85 mm/d.

Table 3 Global mean values of selected parameters of a 30-d forecast of GME ($ni = 128$, 31 layers) for December 1992. Fluxes are 10-d averages, all other values are instantaneous values.

Parameter		**Day 10/ day 0 to day 10**	**day 20/ day 10 to day 20**	**day 30/ day 20 to day 30**
Surface pressure	(hPa)	984.66	984.55	984.44
Temperature at 2m	(°C)	11.84	11.60	11.70
Wind speed at 10 m	(m/s)	5.61	5.68	5.74
Total cloud cover	(%)	68.49	69.11	66.55
Solar radiation balance, top	(W/m^2)	213.00	212.81	213.08
Thermal radiation balance, top	(W/m^2)	-233.64	-233.34	-233.32
Solar radiation balance, bottom	(W/m^2)	135.57	135.37	135.63
Thermal radiation balance, bottom	(W/m^2)	-49.05	-49.64	-49.99
Sensible heat flux, surface	(W/m^2)	-15.37	-15.80	-16.37
Latent heat flux, surface	(W/m^2)	-82.58	-82.33	-82.98
Precipitation	(mm/d)	2.94	2.93	2.95
Evapotranspiration	(mm/d)	2.85	2.84	2.87
Precipitation – Evapotranspiration	(mm/d)	0.09	0.09	0.08

8.3 Precipitation forecast for Oder flood

The flooding at the river Oder and its tributaries caused by a stationary deep low was the most devastating meteorological event in Central Europe in July 1997. During a first period between July 4 to 7 more than 100 mm of precipitation were measured in the area 14 to 20°E, 49 to 52°N (Fig. 20). GME forecasts at two resolutions, namely $ni = 96$ ($\Delta \sim 80$ km) and $ni = 128$ ($\Delta \sim 60$ km), and two forecast ranges (left: +06 to 30h, right: +30 to +54h), both with 31 layers, are compared to observations. Except for the underestimation on the first day (July 4), the amount of precipitation has been properly simulated by GME, especially at the higher resolution $ni = 128$.

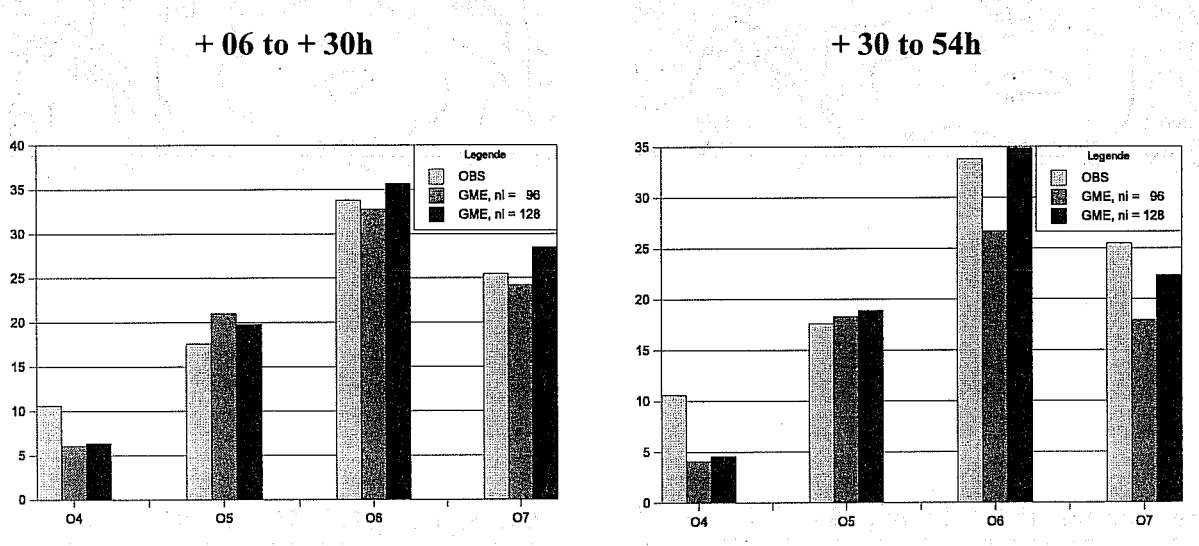

Figure 20 Area mean of total precipitation, July 4 to 7, 1997. Area 14 to 20°E, 49 to 52°N. Observed (Obs) and forcasted by GME (80 and 60 km mesh size, 31 layers). Left: Forecast range +06 to +30h; right: +30 to +54h.

8.4 Pre-operational trial of GME

Since 1st of July 1998 GME ($ni = 128$, 31 layers) is performing 174-h forecasts twice a day based on 00 and 12 UTC analyses. As an example, Fig. 21 shows 132-h forecasts of the mean sea level pressure for the North Atlantic and Western Europe, initialized at 12 UTC on 25 August 1998, for GM (T106), GME and IFS (T_L319, ECMWF) and the verifying analysis. GME has been initialized by an interpolated GM analysis because the full data assimilation scheme of GME will be available by September 1998, only. Even though GME and GM differ completely in numerics and in most physical parameterization schemes their forecasts differ much less from each other than from the IFS forecast. This, once again, indicates the importance of the initial state for the evolution of the forecast in many cases.

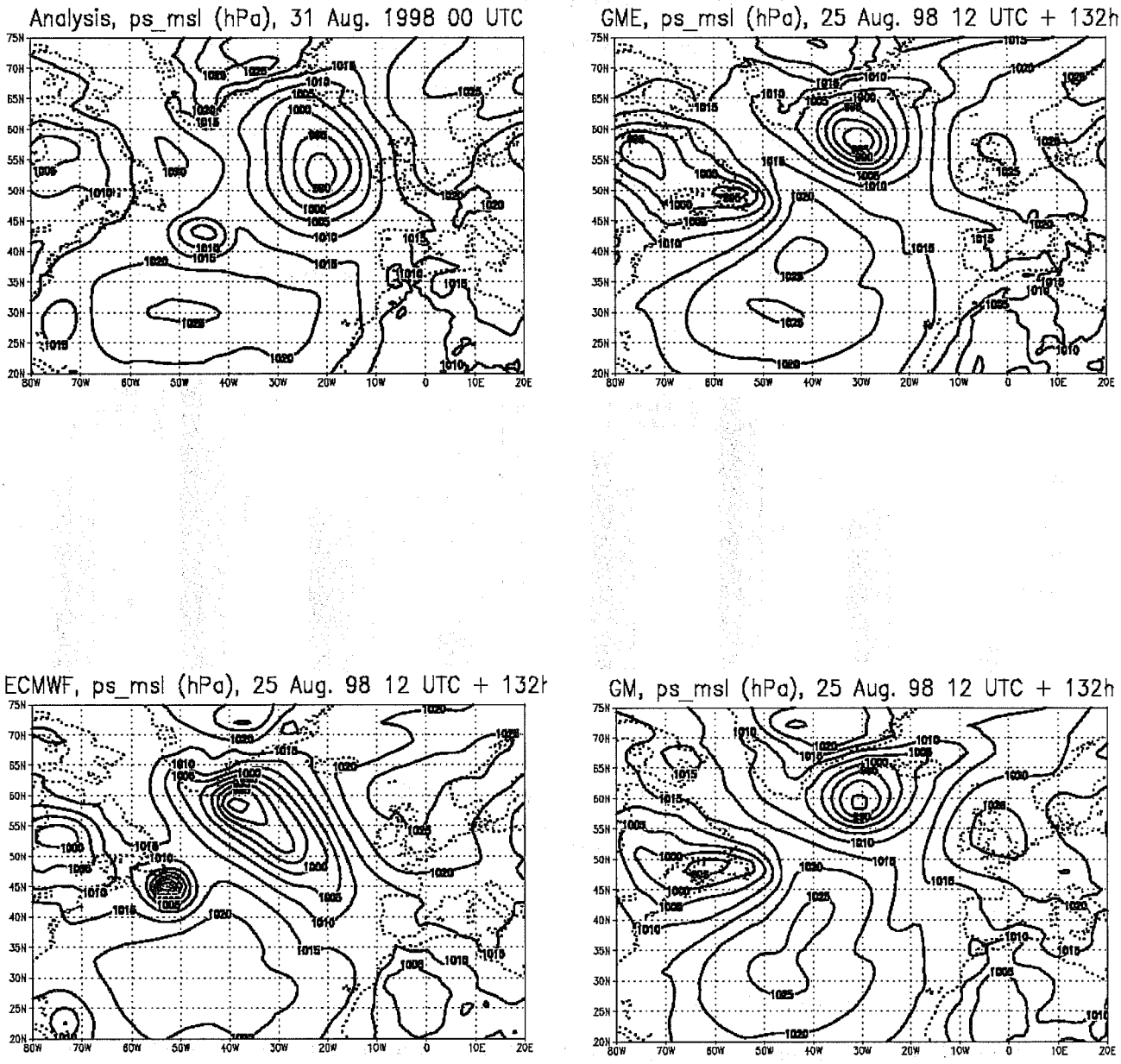

Fig. 21 132-h forecast of pressure at msl (unit: hPa), started at 12 UTC on 25 Aug. 1998.
Top left: Verifying analysis; top right: GME (*ni* = 128, 31 layers);
Bottom left: IFS (T_L319, 31 layers); bottom right: GM (T106, 19 layers).

9. OUTLOOK

GME is the global part of the new numerical weather prediction (NWP) system of DWD (see Tab. 4) which also features the nonhydrostatic regional *Lokal-Modell* LM for Central Europe. Moreover, a relocatable version of LM can be placed anywhere on the globe to serve the needs of the armed forces of Germany. Initially, LM will use a 7-km mesh and 35 layers. By the year 2002 a 2.5-km version with 45 to 50 layers will allow the *explicit prediction of deep convection* and mark the next quantum leap in weather forecasting. By that time, GME with a 30-km mesh and about 35 to 40 layers will use only 10% of the computer resources needed by LM. Thus running a global model which provides the best lateral boundary conditions for the regional model(s) adds almost negligible cost to the overall computational requirements of the NWP system.

Table 4 Fourth NWP system of the Deutscher Wetterdienst

Model	Numerics	Mesh size (km)	# of gridpoints	# of layers	Domain	Lateral boundary
GME	hydrostatic, icosahedral-hexagonal grid, Arakawa-A, Eulerian/semi-Lagrangian, semi-implicit	60	163842	31	global	-
LM	nonhydrostatic, rotated latitude-longitude grid, Arakawa-C, split-explicit (horizontal), implicit (vertical)	7	325 x 325	35	Germany/ surrounding	GME $\Delta t_{LB} = 1$ h

Model	Data assimilation	Initialization	Range
GME	Intermittent 4-dimensional data assimilation based on optimum interpolation (OI), 6-h cycle, 3-h observation window; sea surface temperature analysed at 00 UTC.	Incremental digital filtering initialization, 3-h adiabatic backward integration, 3-h diabatic forward integration, centered at analysis time.	174 h for 00, 12 48 h for 06, 18
LM	Continuous data assimilation based on the nudging method; sea surface temperature analysed at 00 UTC.	Digital filtering initialization, 1-h adiabatic backward integration, 1-h diabatic forward integration, centered at analysis time.	48 h for 00, 06, 12, 18

Acknowledgements

This paper reflects the combined effort of many people at DWD, several universities and research institutions. I am indebted to all of them, especially to

D. Liermann, P. Prohl, B. Ritter and M. Gertz at DWD,

J. Baumgardner at Los Alamos National Laboratories, USA,

P. Lynch at Irish Meteorological Service, Dublin, and

R. Johanni at SGI/Cray, Munich.

References

Baumgardner, J. R., 1983: A three-dimensional finite element model for mantle convection. Thesis, University of California, 271 pp.

Baumgardner, J. R. and P.O. Frederickson, 1985: Icosahedral discretization of the two-sphere. SIAM J. Numer. Anal., Vol. 22, No. 6, 1107-1115.

Dutton, J.A., 1976: The ceaseless wind, McGraw-Hill, Inc., pp 579.

Giraldo, F. X., 1997: Lagrange-Galerkin methods on spherical geodesic grids. J. Comp. Phys., 136, 197-213.

Heikes, R. and D. A. Randall, 1995a: Numerical integration of the shallow-water equations on a twisted icosahedral grid. Part I: Basic design and results of tests. Mon. Wea. Rev., 123, 1862-1880.

Heikes, R. and D. A. Randall, 1995b: Numerical integration of the shallow-water equations on a twisted icosahedral grid. Part II: A detailed description of the grid and an analysis of numerical accuracy. Mon. Wea. Rev., 123, 1881-1887.

Jablonowski, Chr., 1998: Test der Dynamik zweier globaler Wettervorhersagemodelle des Deutschen Wetterdienstes: Der Held-Suarez Test. Diploma thesis, University of Bonn.

Jacobsen, I. and E. Heise, 1982: A new economic method for the computation of the surface temperature in numerical models. Beitr. Phys. Atm., 55, No. 2, 128-141.

Held, I. M. and M. Suarez, 1994: A proposal for the intercomparison of the dynamical cores of atmospheric general circulation models. Bull. Amer. Meteor. Soc., Vol. 75, 10, 1825-1830.

Lott, F. and M. Miller, 1997: A new sub-grid scale orographic drag parameterization: its formulation and testing. Quart. J. Roy. Meteor. Soc., 123, 101-128.

Louis, J.-F., 1979: A parametric model of vertical eddy fluxes in the atmosphere. Boundary-Layer Meteor., 17, 187-202.

Lynch, P., 1997: The Dolph-Chebyshev window: A simple optimal filter. Mon. Wea. Rev., 125, 655-660.

Masuda, Y. and H. Ohnishi, 1986: An integration scheme of the primitive equations model with an icosahedral-hexagonal grid system and its application to the shallow water equations. Proc. WMO/IUGG Symp. on Short- and Medium-Range Numerical Weather Prediction. Tokyo, Japan, Japan Meteorological Society, 317-326.

Mellor, G.L. and T. Yamada, 1974: A hierarchy of turbulence closure models for planetary boundary layers. J. Atmos. Sci., 31, 1791-1806.

Ritter, B. and J.-F. Geleyn, 1992: A comprehensive radiation scheme for numerical weather prediction models with potential applications in climate simulations. Mon. Wea. Rev., 120, 303-325.

Robert, A., 1981: A stable numerical integration scheme for the primitive meteorological equations. Atmos. Ocean, 17, 35-46.

Sadourny, R., A. Arakawa and Y. Mintz, 1968: Integration of the non-divergent barotropic vorticity equation with an icosahedral-hexagonal grid for the sphere. Mon. Wea. Rev., 96, 351-356.

Simmons, A. J. and D. M. Burridge, 1981: An energy and angular-momentum conserving vertical finite-difference scheme and hybrid vertical coordinate. Mon. Wea. Rev., 109, 758-766.

Staniforth, A. and J. Côté, 1991: Semi-Lagrangian integration schemes for atmospheric models – A review. Mon. Wea. Rev., 121, 2206-2223.

Thuburn, J., 1997: A PV-based shallow-water model on a hexagonal-icosahedral grid.
Mon. Wea. Rev., 125, 2328-2347.

Tiedtke, M., 1989: A comprehensive mass flux scheme for cumulus parameterization in large-scale models.
Mon. Wea. Rev., 117, 1779-1800.

Williamson, D. L., 1968: Integration of the barotropic vorticity equation on a spherical geodesic grid.
Tellus, 20, 642-653.

Williamson, D. L., J. B. Drake, J. J. Hack, R. Jakob and P. N. Swarztrauber, 1992: A standard test set for numerical approximations to the shallow-water equations in spherical geometry.
J. Comput. Phys., 102, 221-224.